Fluctuations in the quark-meson model for QCD with isospin chemical potential

Kazuhiko Kamikado[a], Nils Strodthoff[b], Lorenz von Smekal[b], Jochen Wambach[b,c]

[a] *Yukawa Institute for Theoretical Physics, Kyoto University, Kyoto 606-8502, Japan*
[b] *Institut für Kernphysik, Technische Universität Darmstadt, 64289 Darmstadt, Germany*
[c] *GSI Helmholtzzentrum für Schwerionenforschung GmbH, 64291 Darmstadt, Germany*

Abstract

We study the two-flavor quark-meson (QM) model with the functional renormalization group (FRG) to describe the effects of collective mesonic fluctuations on the phase diagram of QCD at finite baryon *and* isospin chemical potentials, μ_B and μ_I. With only isospin chemical potential there is a precise equivalence between the competing dynamics of chiral versus pion condensation and that of collective mesonic and baryonic fluctuations in the quark-meson-diquark model for two-color QCD at finite baryon chemical potential. Here, finite $\mu_B = 3\mu$ introduces an additional dimension to the phase diagram as compared to two-color QCD, however. At zero temperature, the (μ_I, μ)-plane of this phase diagram is strongly constrained by the "Silver Blaze problem." In particular, the onset of pion condensation must occur at $\mu_I = m_\pi/2$, independent of μ as long as $\mu + \mu_I$ stays below the constituent quark mass of the QM model or the liquid-gas transition line of nuclear matter in QCD. In order to maintain this relation beyond mean field it is crucial to compute the pion mass from its timelike correlator with the FRG in a consistent way.

Keywords: QCD phase diagram, isospin density, functional renormalization group.

1. Introduction

The phase diagram of Quantum Chromodynamics (QCD) continues to receive enormous attention both experimentally and theoretically worldwide [1–3]. QCD is expected to reveal a rich phase structure in the plane of temperature T and baryon chemical potential μ_B. Monte-Carlo simulations in lattice gauge theory provide a powerful non-perturbative first principle approach to QCD. At finite baryon chemical potential, however, they are restricted by the fermion-sign problem, the fermion determinant becomes complex, in general, and it can therefore no longer be interpreted as part of a probability measure. There are various ways to deal with the sign problem [4], but the region of large baryon chemical potential and low temperature, $\mu_B \gg T$, essentially remains inaccessible to lattice simulations. This is one motivation to study effective models with QCD symmetries such as (Polyakov-)Nambu-Jona-Lasinio ((P)NJL) [5–7] or (Polyakov-)quark-meson ((P)QM) models [8–11], in order to describe the expected gross features of the QCD phase diagram at finite baryon chemical potential.

The sign problem also motivates studies of QCD-like theories without this problem such as QCD with isospin chemical potential μ_I or two-color QCD [12, 13]. In both cases the fermion determinant remains real, and for an even number of degenerate quark flavors positive at finite density. Consequently, lattice studies can be performed for both, QCD at finite isospin density [14–17] as well as two-color QCD at finite baryon density [18–21]. In both these cases one studies a bosonic superfluid with BEC-BCS crossover towards higher densities in the low temperature, finite density region, however. An interesting QCD replacement with fermionic baryons is the exceptional G_2 gauge theory [22] which can also be simulated at finite density without sign problem [23]. Such lattice simulations allow to benchmark and cross-check the effective model calculations [24] as well as non-perturbative functional continuum methods for full QCD in general [25, 26].

In this letter we use the functional renormalization group (FRG) to study collective mesonic fluctuations in the two-flavor QM model for QCD at finite baryon and isospin chemical potential. As compared to the standard (μ_B, T) phase diagram, finite isospin chemical potential thereby induces an imbalance between up and down quarks as in neutron stars or heavy ion collisions, for example. The region of high baryon density, where this becomes relevant, cannot be described by a QM model without any baryonic degrees of freedom, of course. On the other hand, in color superconducting quark matter at even higher density, isospin chemical potential will eventually destroy BCS pairing probably leading through an FFLO phase into an unpaired state [27, 28]. The other way round, finite baryon or isosymmetric quark chemical potential $\mu = \mu_B/3$ will lead to an imbalance of the Fermi spheres of up and anti-down quarks and thus destroy pion condensation in the (μ_I, T) phase diagram, transgressing through an FFLO phase, likewise [12].

Moreover, the standard QCD phase diagram with baryon chemical potential is related to that with isospin chemical potential outside the pion condensation phase via orbifold equivalence in the large N_c-limit [29]. Just as two-color QCD [13], the latter can be described at sufficiently low temperatures within the framework of chiral effective field theory [12, 30, 31] and random matrix theory [32, 33]. At zero temperature, chiral perturbation theory predicts a second order quantum phase transition at $\mu_I^c = m_\pi/2$, the onset of pion condensation. This is an exact property whose explicit verification from the grand parti-

tion function is called the Silver Blaze problem [34]. It relates the onset of pion condensation to the (vacuum) pion mass m_π. The charged pions couple to $2\mu_I$, so their excitation thresholds are given by $m_\pi \pm 2\mu_I$, and the zero-temperature limit of the partition function must remain independent of μ_I below the critical value of the isospin chemical potential at which $m_\pi - 2\mu_I = 0$. The two-flavor theory at $\mu_I = 0$ is invariant under the full $O(3)$ flavor rotations in π_0, π_+, π_-. Isospin chemical potential is associated with the conserved charge corresponding to the $O(2)$ subgroup of rotations in the π_+, π_- plane. It acts as an external field which explicitly breaks the $O(3)$ down to $O(2)$, but the zero temperature limit of the partition function remains unchanged as long as its strength is not sufficient to excite charged pions. When the isospin chemical potential reaches its critical value at $\mu_I^c = m_\pi/2$, on the other hand, the resulting pionic Nambu-Goldstone excitations of zero energy lead to the spontaneous breaking of the corresponding $O(2)$ symmetry, and Bose-Einstein condensation (BEC) of charged pions occurs.

Considering non-zero values for both isospin and isosymmetric quark chemical potential, more general constraints arise from the Silver Blaze property in the zero temperature (μ_I, μ) phase diagram as we will discuss below. We furthermore present the phase diagram of the QM model for two-flavor QCD in the three-dimensional parameter space of temperature, isospin and isosymmetric quark chemical potential. As compared to previous model studies, mainly within the NJL model [35–43], the FRG approach is thereby well equipped to include the corresponding collective mesonic fluctuations in the description of chiral versus pion condensation.

2. Quark-meson model with isospin chemical potential

With the standard two-flavor chiral symmetry-breaking pattern, $SU(2)_L \times SU(2)_R \to SU(2)_V$, finite isospin chemical potential leads to a further explicit breaking of the $SU(2)_V$ isospin symmetry down to the rotations about the iso-three direction, *i.e.*, on the quark level to $SU(2)_V \to U(1)_V^{(3)}$. In the pion condensation phase at $\mu_I \geq \mu_I^c(T)$, with $\mu_I^c(0) = m_\pi/2$, this remnant chiral symmetry then spontaneously breaks down to a discrete Z_2 symmetry, $U(1)_V^{(3)} \to Z_2$, with a non-vanishing pion-condensate as the order parameter and one Nambu-Goldstone boson. As the isospin chemical potential is further increased, the pion condensate increases and the chiral condensate decreases corresponding to a rotation of the vacuum alignment in a BEC-BCS crossover. The approximate chiral symmetry gets partially restored, and the asymptotic $Z_2 \times U(1)_A^{(3)}$ symmetry for $\mu_I \to \infty$ in the pion condensation phase agrees with that obtained in a hypothetical world with isospin chemical potential but without any chiral symmetry breaking (χSB) and hence quark mass $m_q = 0$ as summarized in Table 1.

	with χSB	without χSB	
	$SU(2)_L \times SU(2)_R$	$SU(2)_L \times SU(2)_R$	
$m_q \neq 0$	$\downarrow$	$\downarrow$	$\mu_I \neq 0$
	$SU(2)_V$	$U(1)_L^{(3)} \times U(1)_R^{(3)}$	
$\mu_I \neq 0$	$\downarrow$	$\downarrow$	SSB
	$U_V(1)$	$Z_2 \times U(1)_A^{(3)}$	
SSB	$\downarrow$		
	Z_2		

Table 1: Symmetry breaking patterns in the charged pion condensation phase.

In this letter we use the QM model as a chiral effective model in which this symmetry pattern is realized. The Euclidean Lagrangian of the QM model at finite quark chemical potential $\mu = \mu_B/3$ but zero isospin chemical potential is given by

$$\begin{aligned}\mathcal{L}_{\rm QM} &= \bar{\psi}\left(\partial\!\!\!/ + g(\sigma + i\gamma_5\vec{\tau}\vec{\pi}) - \mu\gamma_0\right)\psi \\ &\quad + \frac{1}{2}(\partial_\mu\sigma)^2 + \frac{1}{2}(\partial_\mu\vec{\pi})^2 + U(\sigma^2+\vec{\pi}^2) - c\sigma,\end{aligned} \tag{1}$$

with mesonic potential $U(\sigma^2+\vec{\pi}^2) = \frac{m^2}{2}(\sigma^2+\vec{\pi}^2) + \frac{\lambda}{4!}(\sigma^2+\vec{\pi}^2)^2$ and explicit χSB term $c\sigma$ corresponding to a finite current quark mass. The Lagrangian is invariant under $O(3)$-isospin rotations. For the iso-three direction these are of the form

$$\psi \to e^{i\tau_3\theta}\psi, \quad \psi^\dagger \to e^{-i\tau_3\theta}\psi^\dagger, \quad \pi_\pm \equiv \pi_1 \pm i\pi_2 \to e^{\mp i2\theta}\pi_\pm, \tag{2}$$

with an associated conserved current

$$J_\mu^3 = i\bar{\psi}\tau_3\gamma_\mu\psi + 2i(\pi_-\partial_\mu\pi_+ - \pi_+\partial_\mu\pi_-). \tag{3}$$

Isospin chemical potential is now introduced in the usual way, by adding a term $\mu_I Q^3$ with the associated conserved charge to the corresponding Hamiltonian. Following the standard derivation [44], one obtains the Lagrangian with finite isospin and isosymmetric quark chemical potential, conveniently written in the basis of up and down quarks with $\psi = (\psi_u^T, \psi_d^T)^T$ as

$$\begin{aligned}\mathcal{L}_{QM+\mu_I} =& \bar{\psi}S_0^{-1}\psi + \frac{1}{2}(\partial_\mu\sigma)^2 + \frac{1}{2}(\partial_\mu\pi_0)^2 + U(\rho^2, d^2) - c\sigma \\ &+ \frac{1}{2}\left((\partial_\mu + 2\mu_I\delta_\mu^0)\pi_+(\partial_\mu - 2\mu_I\delta_\mu^0)\pi_-\right),\end{aligned} \tag{4}$$

where $\rho^2 \equiv \sigma^2 + \pi_0^2$ (with $\pi_0 \equiv \pi^3$), $d^2 \equiv \pi_+\pi_-$, and

$$S_0^{-1} = \begin{pmatrix} \partial\!\!\!/ + g(\sigma + i\gamma_5\pi_0) - (\mu+\mu_I)\gamma_0 & gi\gamma_5\pi_- \\ gi\gamma_5\pi_+ & \partial\!\!\!/ + g(\sigma - i\gamma_5\pi_0) - (\mu-\mu_I)\gamma_0 \end{pmatrix}. \tag{5}$$

Setting $\mu = 0$ temporarily, it is evident in this representation that there is a precise map between the quark-meson model for QCD with isospin chemical potential μ_I and the corresponding quark-meson-diquark model for two-color QCD [45] with baryon chemical potential provided by the following modifications: Instead of the bi-spinors in flavor here, one introduces bi-spinors in color consisting of say a red quark ψ_r and a green charge-conjugated antiquark $\psi_g^C \equiv \tau_2 C\bar{\psi}_g^T$, with τ_2 for complex conjugation in the flavor $SU(2)$. The charged pions π_- and π_+ are then replaced by a scalar diquark-antidiquark pair, Δ and Δ^*, coupled to the baryon chemical potential $\mu_B = 2\mu$ for $N_c = 2$ instead of $2\mu_I$ for the charged pions in QCD with isospin chemical potential, and the neutral pion π_0 is replaced by the isovector of three pions $\vec{\pi}$, with $\pi_0 \to \vec{\tau}\vec{\pi}$ in S_0^{-1}, which increases the number of would-be-Goldstone bosons for χSB from 3 to 5 in two-color QCD with two flavors. This identification is valid only for the matter sector, of course, as the gauge sectors of both theories are fundamentally different.

3. FRG flow equations

3.1. Effective potential

The functional renormalization group is a well-established non-perturbative tool to study critical phenomena in quantum field theory and statistical physics. It describes the evolution of the scale-dependent effective average action Γ_k from a microscopic bare action specified at a UV cutoff scale Λ_{UV} to the full quantum effective action for $k \to 0$ in terms of a functional differential equation [46]

$$\partial_k \Gamma_k[\phi] = -\mathrm{Tr}\left[\frac{\partial_k R_{k\mathrm{F}}}{\Gamma_k^{(2,0)} + R_{k\mathrm{F}}}\right] + \frac{1}{2}\mathrm{Tr}\left[\frac{\partial_k R_{k\mathrm{B}}}{\Gamma_k^{(0,2)} + R_{k\mathrm{B}}}\right], \quad (6)$$

where $\Gamma_k^{(n,m)}$ denotes the n th functional derivative with respect to fermionic and m th functional derivative with respect to bosonic fields of the effective average action and the trace is taken over internal degrees of freedom and momentum space. Fig. 1 shows a diagrammatic representation of Eq. (6). Although the flow equation has one loop structure, it is exact. Apart from the general requirements to act as the desired infrared regulator consistent with the boundary conditions [47, 48], there is a certain freedom in the precise choice of the fermionic/bosonic regulator functions $R_{k\mathrm{F}}/R_{k\mathrm{B}}$ which can be exploited to minimize truncation effects. Here we use

$$R_{k\mathrm{B}} = (k^2 - \vec{p}^2)\theta(k^2 - \vec{p}^2), \quad (7)$$

$$R_{k\mathrm{F}} = \not{p}\left(\sqrt{\frac{k^2}{\vec{p}^2}} - 1\right)\theta(k^2 - \vec{p}^2), \quad (8)$$

which are three-momentum analogues of the optimized regulator for the local potential approximation (LPA) [49]. They have the particular advantage that the Matsubara sums in the flow can be evaluated analytically. The regulators suppress the propagation of momentum modes below the scale k. Quantum fluctuations from all momentum modes are included by integrating the flow equation (6) from the bare classical action at Λ_{UV} down to $k = 0$. From n functional derivatives of (6) one obtains the flow equations for the n-point vertex functions which in turn contain up to $(n+2)$-point functions. Just as Dyson-Schwinger equations, the flow equations for all n-point functions form an infinite hierarchy which requires truncations to obtain a closed system of equations suitable for non-perturbative solutions.

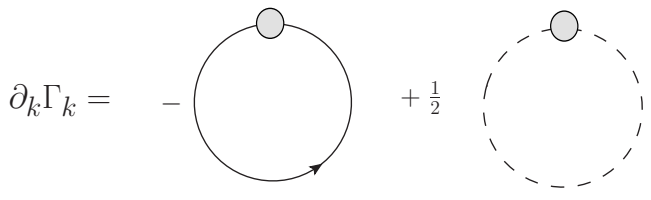

Figure 1: Diagrammatic representation of the flow equation for the effective action. Solid (dashed) lines represent full field and RG scale k dependent fermion (boson) propagators and the circles insertions of $\partial_t R_k(q)$.

One frequently used truncation scheme is the derivative expansion, which has been applied successfully to $O(N)$ and quark-meson models. In contrast to the NJL model, the QM model contains explicit mesonic degrees of freedom in the Lagrangian and is well suited to study mesonic fluctuations with the FRG. At leading order in the derivative expansion a scale-dependent effective potential U_k is obtained without wave function renormalizations and with scale-independent Yukawa couplings. The Ansatz for the scale-dependent effective action is chosen to comply with the expected symmetry-breaking pattern. In particular, because isospin chemical potential explicitly breaks the $O(4)$ flavor symmetry of the mesonic sector down to $O(2)\times O(2)$, the effective potential U_k must be allowed to depend on two invariants, $\rho^2 = \sigma^2 + \pi_0^2$ and $d^2 = \pi_1^2 + \pi_2^2 = \pi_+\pi_-$. Therefore, our Ansatz for the effective action is given by

$$\Gamma_k[\rho^2, d^2] = T\sum_n \int \mathrm{d}^3x \, \mathcal{L}_{QM+\mu_I}\big|_{U\to U_k(\rho^2,d^2)}, \quad (9)$$

with $\mathcal{L}_{QM+\mu_I}$ from Eq. (4). At the UV cutoff scale we assume an $O(4)$ symmetric potential of the form

$$U_{\Lambda_{\mathrm{UV}}} = a\left(\rho^2 + d^2\right) + b\left(\rho^2 + d^2\right)^2. \quad (10)$$

Inserting the Ansatz (9) into the Wetterich equation (6), the flow equation for the effective potential can then be derived entirely analogously to that of the quark-meson-diquark (QMD) model for two-color QCD [45], yielding,

$$k\partial_k U_k = \frac{k^5}{12\pi^2}\left[\frac{1}{E_\pi}\coth\left(\frac{E_\pi}{2T}\right) + \sum_{i=0}^{2}\frac{R_i}{\omega_i}\coth\left(\frac{\omega_i}{2T}\right) - N_c\sum_{\pm}\frac{2}{E_\pm}\left(1 \pm \frac{\mu_I}{E_q}\right)\left(\tanh\left(\frac{E_\pm + \mu}{2T}\right) + \tanh\left(\frac{E_\pm - \mu}{2T}\right)\right)\right]. \quad (11)$$

Here, $E_\pm$ denote k-dependent quark excitation energies,

$$E_\pm = \sqrt{g^2d^2 + (E_q \pm \mu_I)^2}, \quad \text{with} \quad E_q = \sqrt{k^2 + g^2\rho^2}, \quad (12)$$

and for the neutral pion, we introduced

$$E_\pi = \sqrt{k^2 + 2U_r}, \quad (13)$$

with $U_r \equiv \frac{\partial U_k}{\partial \rho^2}$, $U_d \equiv \frac{\partial U_k}{\partial d^2}$, and $U_{rr} \equiv \frac{\partial^2 U_k}{(\partial \rho^2)^2}$, etc. used as shorthand notations for the derivatives of the scale-dependent effective potential here and below. The ω_i are the positive square-roots of the three poles in $\omega^2 = -p_0^2$ of the scale-dependent boson propagator in the 3×3 subspace of π^+, π^- and σ mesons which mix at finite isospin density. They are the roots of the same cubic polynomial as given for the QMD model in [24, 45], and the R_i are the corresponding residues. For $d^2 = \pi_+\pi_- = 0$, without pion condensation and pionic fluctuations, one has $\omega_0 = E_\sigma = \sqrt{k^2 + 2U_r + 4\rho^2 U_{rr}}$, $R_0 = 1$ for the sigma meson, and $\omega_{1,2} = E_\pi \pm 2\mu_I$ with $R_{1,2} = \omega_{1,2}/E_\pi$ for the charged pions.

For zero isosymmetric quark or baryon chemical potential, $\mu = 0$, Eq. (11) is identical to the corresponding flow equation for the effective potential of the QMD model for two-color QCD at finite baryon density [45] with $N_c = 2$, $\mu_I \to \mu$, and a multiplicity of 3 for the first term on the right in Eq. (11) to account for the usual three pions replacing the neutral one here.

3.2. Pion pole mass and flow of the 2-point function

It is common practice in quark-meson model studies to fix the parameters by adjusting the eigenvalues of the Hessian of the effective potential at its minimum to the physical meson masses. We refer to these masses as the screening masses here. They determine the spacelike static limit of the mesonic 2-point functions and thus the inverse of the corresponding susceptibilities. These are not the physical masses, in general. With Bose-Einstein condensation of diquarks in two-color QCD or charged pions here, however, the zero temperature onset at $m_\pi/2$ provides an exact definition of the physical pion mass which is manifestly different from its screening mass [45]. The two differ by the amount by which the radiative corrections change when extrapolating the pion propagator from $p^2 = 0$ to the pion pole at $-p^2 = m_\pi^2$. This is all well-known, of course. Perhaps surprisingly, however, the independent exact mass definition via the quantum phase transition shows that the standard mass assignment in QM models can be off by as much as 30% [45]. The approximation to mistake the pion screening mass for the physical one thus has a considerable Silver Blaze problem.

In general, for more realistic model parameters, independent of the existence of a quantum phase transition, one therefore needs to consider the poles in the zero-temperature propagators or, equivalently, the zeros in the corresponding 2-point functions, to define the physical masses. They are determined from the asymptotic behavior of the propagators at large Euclidean times. For the lowest stable particle it suffices to solve analytically continued flow equations at timelike total momenta, and find, *e.g.*, for the pion,

$$\Gamma_\pi^{(0,2)}(p;\sigma_{\min})\Big|_{-p^2=m_\pi^2} = 0. \tag{14}$$

At mean-field level, the Silver Blaze problem requires this pion pole mass to be computed from the random phase approximation (RPA). It is then guaranteed to agree with the critical chemical potential at the BEC quantum phase transition in NJL and QM models [45, 50]. Here, we use the FRG to calculate a pion pole mass in a way consistent with the derivative expansion of the effective average action. Although an analogous flow equation can be obtained for the 2-point function of the sigma, a pole mass determination requires more work in that case and will not be done here. The additional complication is associated with the finite width of the sigma meson from its decay into two pions, which requires a more careful search for the sigma pole on the correct sheet in the complex plane.

Applying two functional derivatives to Eq. (6), one obtains the flow equations for the 2-point functions as sketched in Fig. 2, which depend on scale-dependent 3- and 4-point functions with their own flow equations. Truncations are necessary in order to close this infinite tower of equations for all n-point functions.

One example of such a truncation scheme is the so-called BMW approximation [51, 52]. The basic idea is that, because of the insertion of the regulator function, the dependence of scale-dependent 3- and 4-point functions on the external momenta is weaker than on the loop momentum. This motivates to expand 3- and 4-point functions in their external momenta.

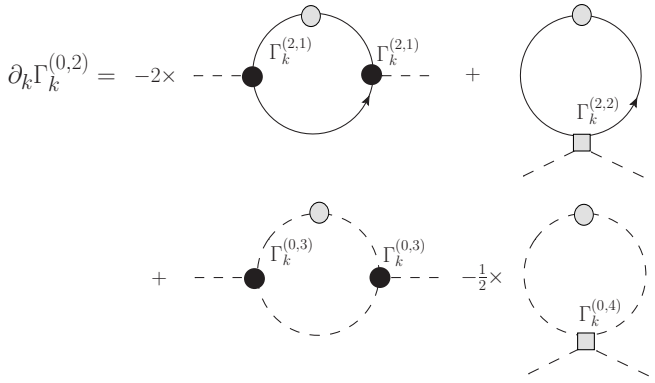

Figure 2: Diagrammatic representation of the flow equation for a mesonic 2-point function. Solid (dashed) lines represent scale-dependent fermion (boson) propagators and the light circles the insertions of $\partial_t R_k(q)$.

At leading order this yields, *e.g.*, for the mesonic 3- and 4-point functions,

$$\Gamma_{ijl}^{(0,3)}(p,-p) = \frac{\partial\Gamma_{ij}^{(0,2)}(p;\phi)}{\partial\phi_l}, \quad \Gamma_{ijlm}^{(0,4)}(p,-p,0) = \frac{\partial^2\Gamma_{ij}^{(0,2)}(p;\phi)}{\partial\phi_m\partial\phi_l}.$$

The resulting closed coupled system of flow equations for the 2-point correlation functions has been studied for example for scalar models in [53, 54]. Consistency between the BMW and LPA approximations for vanishing external momentum, where the 2-point function can also be obtained from derivatives of the effective potential, is not guaranteed, however.

Therefore, we use an even simpler truncation which is manifestly consistent with the leading order in the derivative expansion for the effective average action. This is achieved by using the scale dependent but momentum independent mesonic 3- and 4-point vertices from the computation of the scale dependent effective potential in the flow for the 2-point functions, *i.e.*,

$$\Gamma_{k,\,ijl}^{(0,3)} \equiv \frac{\partial^3 U_k}{\partial\phi_l\partial\phi_j\partial\phi_i}, \quad \Gamma_{k,\,ijlm}^{(0,4)} \equiv \frac{\partial^4 U_k}{\partial\phi_m\partial\phi_l\partial\phi_j\partial\phi_i}. \tag{15}$$

With constant Yukawa coupling at the leading order derivative expansion the quark-meson vertices take their simple RPA forms as in the NJL model [55],

$$\Gamma_0^{(2,1)} = g, \quad \Gamma_i^{(2,1)} = ig\gamma_5\tau_i, \quad \Gamma_{ij}^{(2,2)} = 0. \tag{16}$$

The momentum dependence of the 2-point correlation function now arises entirely from the external momentum through the propagators in the loop. For the vacuum pion mass at zero isospin and baryon chemical potential the effective potential remains $O(4)$ symmetric. We therefore replace $U_k(\rho^2, d^2)$ by $U_k(\phi^2)$ with $\phi^2 = \rho^2 + d^2$ in our Ansatz for the effective average action. The LPA-like flow of the pion 2-point function for

Euclidean external momentum $p = (p_0, \vec{0})$ then becomes,

$$k\partial_k \Gamma^{(0,2)}_{k,\pi}(p_0;\phi) = \frac{k^5}{6\pi^2}\Bigg(-\frac{(N+1)U_k''}{E_\pi^3} - \frac{U_k'' + 2\phi^2 U_k'''}{E_\sigma^3} + \frac{2U''(E_\sigma^2 - E_\pi^2)\left((E_\sigma+E_\pi)^3(E_\sigma^2+E_\sigma E_\pi+E_\pi^2)+(E_\sigma^3+E_\pi^3)p_0^2\right)}{E_\pi^3 E_\sigma^3((E_\pi+E_\sigma)^2+p_0^2)^2} + \frac{8N_f N_c g^2(4E_q^2 - p_0^2)}{E_q\left(4E_q^2+p_0^2\right)^2}\Bigg), \tag{17}$$

with standard primes for the ϕ^2-derivatives here in the place of the ρ^2 and d^2-derivatives of $U_k(\rho^2, d^2)$ above, and $E_\pi = \sqrt{k^2 + 2U'}$, $E_\sigma = \sqrt{k^2 + 2U' + 4\phi^2 U''}$ correspondingly. We use $N = 4$ for the bosonic $O(4)$ symmetry with $N_f = 2$ flavors (as compared to $N = 6$ with $N_f = 2$ in two-color QCD [45]). At zero pion momentum one easily verifies that Eq. (17) agrees with the flow equation for $2U_k'$ obtained from Eq. (11).

We solve the flow equation for the real-time 2-point function by analytically continuing $-p_0^2 = \omega^2 + i\varepsilon$ in Eq. (17) before the integration of the flow equation. The initial condition in the UV is then chosen to be

$$\Gamma^{(0,2)}_{\Lambda_{\rm UV},\pi}(-i\omega;\phi) = -\omega^2 + 2U'_{\Lambda_{\rm UV}}(\phi^2). \tag{18}$$

3.3. Extended mean-field (eMF) approximation

A worthwhile further simplification of the flow equations for the effective potential in Eq. (11) and the 2-point function in Eq. (17) is to consider the purely fermionic flow, *i.e.*, to neglect the mesonic contributions to the flow. This is occasionally being referred to as *extended* mean-field approximation (eMF) in the FRG literature because the fermionic flow is independent of the mesonic potential. Moreover, it provides a convenient way to include vacuum contributions which affect the usual mean-field studies [45, 56]. The corresponding flow equations can then formally be integrated, yielding for the effective potential at finite temperature, isospin and quark chemical potential,

$$U(\rho^2, d^2) = U_\Lambda + \frac{N_c}{6\pi^2}\sum_\pm \int_0^\Lambda dk \frac{k^4}{E_\pm}\left(1 \pm \frac{\mu_I}{E_q}\right) \times \left(\tanh\left(\frac{E_\pm + \mu}{2T}\right) + \tanh\left(\frac{E_\pm - \mu}{2T}\right)\right), \tag{19}$$
$$U_\Lambda = a(\rho^2 + d^2) + b\left(\rho^2 + d^2\right)^2 - c\sigma - 2\mu_I^2 d^2,$$

and for the vacuum pion 2-point function,

$$\Gamma^{(0,2)}_\pi(-i\omega;\sigma) = \frac{4g^2 N_c N_f}{3\pi^2}\int_0^\Lambda dk k^4 \frac{4E_q^2 + \omega^2}{E_q\left(4E_q^2 - \omega^2 - i\varepsilon\right)^2} + \Gamma^{(0,2)}_{\Lambda,\pi},$$
$$\Gamma^{(0,2)}_{\Lambda,\pi} = -\omega^2 + 2a + 4b\sigma^2. \tag{20}$$

As before, the real-time result is obtained via analytic continuation with $-p_0^2 = \omega^2 + i\varepsilon$ from the Euclidean correlation function.

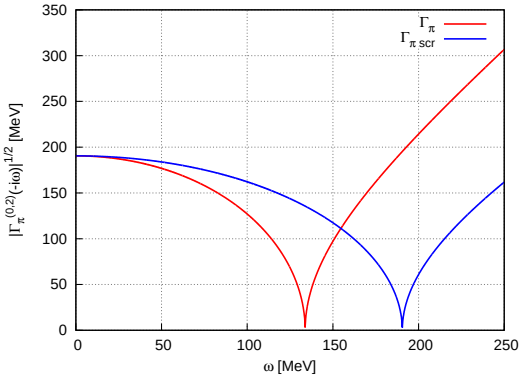

Figure 3: Vacuum pion 2-point correlation function from the full FRG Eq. (17) as a function of timelike $\omega = ip_0$ compared to $\Gamma^{(0,2)}_{\pi,\rm scr}(-i\omega) \equiv -\omega^2 + m_\pi^{\rm scr\,2}$ with the screening mass $m_\pi^{\rm scr} = \sqrt{2U'}$, both from the FRG parameter set C in Tab. 3.

4. Results

We solve the flow equations Eq. (11) and Eq. (17) numerically on grids in field space. For example, in the $O(4)$ symmetric case for $U_k(\phi^2)$ and $\Gamma^{(0,2)}_{k,\pi}(p;\phi)$ this is a one-dimensional set of discrete field values of ϕ^2. The necessary derivatives of the effective potential can be obtained from finite differences or spline interpolations. This leads to a system of ordinary differential equations which can be integrated with standard methods. In comparison to using Taylor expansions of the effective potential around a scale dependent minimum, it captures the form of the effective potential everywhere on the grid in field space instead of being restricted to some region around the minimum. It is thus well suited to describe first order phase transitions. Only recently this technique has been applied to problems with effective potentials depending on several invariants [45]. We use the same techniques here when we study the full two-dimensional flow from Eq. (11) for $U_k(\rho^2, d^2)$ with collective fluctuations in both, the chiral and the charged pion condensate.

4.1. Pole mass versus screening mass

Fig. 3 shows the square root of the modulus of the pion correlation function evaluated at the minimum of the effective potential $\sigma_{\rm min}$ as a function of timelike external $\omega = ip_0$. For comparison, the corresponding $\Gamma^{(0,2)}_{\pi,\rm scr} \equiv -\omega^2 + m_\pi^{\rm scr\,2}$ with the screening mass $m_\pi^{\rm scr}$ from the curvature of effective potential is also shown. Pole and screening mass are the zeros of $\Gamma^{(0,2)}_\pi(-i\omega;\sigma_{\rm min})$ and $\Gamma^{(0,2)}_{\pi,\rm scr}(-i\omega;\sigma_{\rm min})$. Moreover, from Eqs. (11) and (17), $m_\pi^{\rm scr\,2} = \Gamma^{(0,2)}_{\pi,\rm scr}(0;\sigma_{\rm min}) = \Gamma^{(0,2)}_\pi(0;\sigma_{\rm min})$, in our truncation.

In the present example, the pole mass is $m_\pi^{\rm pole} = 133.0$ MeV which is within 3% of the correct value as defined by the quantum phase transition at $2\mu_I^c = 136.6$ MeV with the parameters used here. The screening mass, on the other hand, is much heavier, with $m_\pi^{\rm scr} = 188.0$ MeV it overestimates the correct value by about 38%. The Silver Blaze relation $m_\pi = 2\mu_I^c$ is satisfied exactly for the pion pole mass in the eMF calculation, as it must [45]. For a full FRG calculation, the pion pole mass in our truncation is close and represents a considerable improvement as compared to the screening mass. Perfect agreement should

not be expected in this calculation for the pion pole mass either, since the truncation for the flow of the 2-point function goes beyond the leading order derivative expansion. One possible further improvement, for example, would therefore be to feed the momentum dependent propagators back into the flow equation for the effective potential and obtain both in an iterative procedure. Maybe more importantly, however, these results once more demonstrate that assigning physical values to the screening masses is a rather poor way of fixing model parameters. This is even more so for the pion mass with 3 colors here than it is in the corresponding 2-color calculation [45].

Less pronounced, the same inconsistency between screening mass and quantum phase transition at $\mu = \mu_I^c$ has been observed already in a purely bosonic model with isospin chemical potential [57]. For a screening mass of $m_\pi^{\rm scr} = 138$ MeV, the zero-temperature onset of pion condensation is observed in this model at $2\mu_I^c = 132.6$ MeV, corresponding to a moderate mismatch of 4%. For comparison, we obtain a pion pole mass of $m_\pi^{\rm pole} = 129.9$ MeV in our truncation for this purely bosonic model. The resulting deviation of only 2% again represents at least some improvement as compared to the screening mass. The relatively small deviation of pole and screening masses here is in line with the general observation that fermions provide the dominant contributions to the flow in QM models.

4.2. Parameter fixing

eMF calculation. For the extended mean-field calculation, we select parameter sets A, B, C and D which reproduce the pion decay constant f_π and the pion pole mass and in the vacuum from Eqs. (19) and (20), as summarized in Tab. 2. In this range of parameters the mass m_σ of the sigma meson increases monotonically with the quartic coupling b in the UV potential.

	a/Λ^2	b	c/Λ^3	f_π	$m_\pi^{\rm pole}$	$m_\sigma^{\rm scr}$
A	0.245	1.0	0.0124	92.8	138	457
B	0.196	2.0	0.0123	92.9	137	504
C	0.09	4.0	0.0125	92.4	138	698
D	-0.09	8.0	0.0125	92.8	139	868

Table 2: Parameters for eMF calculations with UV cutoff $\Lambda = 600$ MeV and Yukawa coupling $g = 3.2$; f_π and meson masses are given in MeV.

The left panel in Fig. 4 shows the resulting (μ, T) phase diagram with $\mu_I = 0$ and no pion condensation. For the parameter sets A and B there is a critical endpoint (CEP) at $(T, \mu) =$ (22.5 MeV, 314 MeV) and (32 MeV, 295 MeV), respectively. The position of the CEP is very sensitive to the choice of parameters. With increasing m_σ the CEP moves to lower temperatures and eventually disappears from the phase diagram beyond a critical value of $m_\sigma^{\rm scr\,*} \sim 550$ MeV, so there is none for parameter sets C and D. A similar behavior was observed in a mean-field 3-flavor QM model calculation [58]. An intuitive understanding of this effect is gained by considering a Landau expansion of the effective potential in σ^2, yielding,

$$U(\sigma, T, \mu) = a'(T,\mu)\sigma^2 + b'(T,\mu)\sigma^4 + d(T,\mu)\sigma^6, \qquad a'(T,\mu) = a(T,\mu) + a, \quad b'(T,\mu) = b(T,\mu) + b. \tag{21}$$

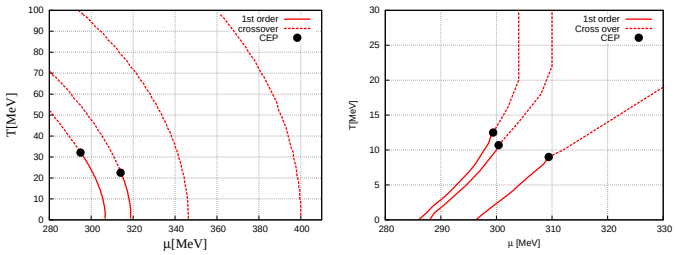

Figure 4: QM model phase diagram at $\mu_I = 0$ from eMF (left, parameter sets A,B,C, D from left to right) and full FRG (right, parameter sets A,B,C) calculations. Solid lines represent first order phase boundaries and dashed lines trace minima in the screening mass of the sigma meson to indicate chiral crossovers.

To describe a first order phase transition we need to keep terms up to sixth order. The corresponding quark contributions are $a(T,\mu)$, $b(T,\mu)$ and $d(T,\mu)$. They are independent of the initial parameter choices for a and b. Around the first order phase boundary, the total coefficients satisfy $a' > 0$, $b' < 0$ and $d > 0$, which is just the condition for a double-well. For a sufficiently large quartic bare coupling b, this condition can no longer be satisfied. Thus the first order phase transition and the CEP have to disappear from the (μ, T) phase diagram as m_σ increases.

The UV cutoff scale of $\Lambda = 600$ MeV, which we use for the eMF calculation here, allows a most direct comparison with earlier mean-field results. From these it is known that vacuum contributions have a considerable effect on the chiral first order line and CEP [56]. For standard mean-field calculations vacuum terms with a sharp 600 MeV cutoff were found to well reproduce cutoff-independent results in dimensional regularisation [45]. The eMF results include such contributions by construction. They are therefore best compared to those earlier calculations when one starts the fermionic flow at 600 MeV also.

However, while eMF results for a given fixed sigma mass are practically cutoff independent, sigma masses as low as those with sets A and B in Tab. 2 are not possible for larger UV cutoff scales such as the 900 MeV used in the FRG results below. This is due to an emerging instability in the UV potential, with $b < 0$ in (21). As a result, we are then unable to reach sigma masses below the $m_\sigma^{\rm scr\,*} \sim 550$ MeV needed for a chiral first order transition and CEP. For a comparison with the full FRG results below it therefore also seems more appropriate to keep the lower cutoff in the eMF calculations. The main focus of this letter, the pion condensation phase at finite isospin chemical potential, however, is not affected by this choice. The eMF results in this region of the phase diagram remain essentially unchanged when we go to the 900 MeV UV cutoff scale.

FRG calculation. Three sets for initial parameters in full FRG solutions are listed in Tab. 3. As for the eMF results, the screening mass of the sigma monotonically increases with the quartic coupling parameter b.

The right panel in Fig. 4 shows the $\mu_I = 0$ phase diagram in the (μ, T) plane in the vicinity of the CEP for the three parameter sets A,B and C. In contrast to the eMF calculation, the phase structure for all sets is quite similar, although the screening masses are rather different. In all cases there are first order

	a/Λ^2	b	c/Λ^3	f_π	$m_\pi^{\rm pole}$	$m_\sigma^{\rm scr}$
A	0.3224	0.25	0.0045	93.3	134.3	524.1
B	0.2844	1.25	0.0045	92.8	134.1	557.1
C	0	9.075	0.0045	92.8	133	696.7
A'	-0.48	9.74	0.0024	93.0	138.0	448

Table 3: Initial parameters for full FRG calculations (parameter set A' for the purely bosonic model). The UV cutoff is set to $\Lambda = 900$ MeV and $g = 3.2$; f_π and meson masses are given in MeV.

phase transitions and CEPs. In the full FRG effective potential, it makes no sense to separate the initial potential from the contributions due to fluctuations as in Eq. (21). Differences at the UV scale are reduced by the mesonic fluctuations. As a result, the phase structure from full FRG calculations is less sensitive to the resulting sigma mass than in mean-field calculations.

4.3. Zero temperature phase diagram

First consider the zero temperature quantum phase transition with pion condensation at $\mu = 0$. We have calculated the isospin density from the μ_I-derivative of the effective potential. The result is shown in Fig. 5 where the rescaled isospin chemical potential $2\mu_I/m_\pi$ is plotted over the isospin density ρ_I for our eMF and FRG solutions in comparison with very recent lattice data from Ref. [17] and the leading order chiral effective field theory (χPT) result [12]. The isopin density remains zero below the onset of pion condensation at $\mu_I^c = m_\pi/2$ in the eMF calculation as it must while the full FRG result shows a slight residual Silver Blaze problem here, which might be due to numerical integration and infrared cutoff uncertainties. For large μ_I, deep into the pion condensation phase, it gets increasingly difficult to control systematic errors in the full FRG calculations, *e.g.*, because the assumption of μ_I-independent initial parameters at a fixed ultraviolet cutoff breaks down eventually.

While the chiral effective field theory result describes the BEC phase well, it appears to miss some essential dynamics in the BEC-BCS crossover, which we estimate to occur around $2\mu_I/m_\pi - 1 \approx 2/3$ in our calculations by the simple criterion that the quarks' Dirac mass falls below μ_I there. Because the vacuum realignment in this crossover is characterized by the mixing between the sigma meson with the charged pions in the QM model, this suggests that it might indeed be this mixing of the meson mass eigenstates which is responsible for the observed inflection point and back-bending of the isospin density at large μ_I. The analogous mixing is seen in the mass spectrum of the QMD model for two-color QCD [45], between diquarks and the sigma meson. Basically, the latter is infinitely heavy in χPT, so the low-lying excitation spectrum of the QM model is essentially different from that of the non-linear sigma model, especially in the crossover region where the mixing occurs. The qualitative effect on the isospin density can be illustrated in the *linear* sigma model, where a simple calculation yields,

$$\rho_I(x,y) = 2 f_\pi^2 m_\pi \, x \left(\frac{y^2-3}{y^2-1} - \frac{1}{x^4} + \frac{2}{y^2-1} x^2 \right), \qquad (22)$$

for $x \equiv 2\mu_I/m_\pi \geq 1$, and with $y \equiv m_\sigma/m_\pi$. In the $y \to \infty$ limit, this reduces to the χPT result $\rho_I(x) = 2 f_\pi^2 m_\pi \, x(1 - x^{-4})$ [12].

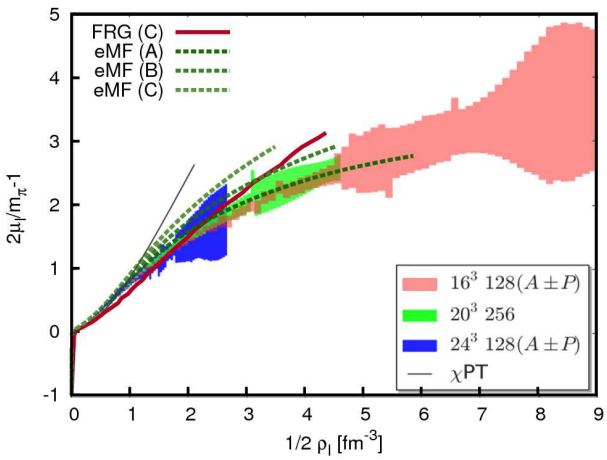

Figure 5: Isospin chemical potential over isospin density at zero temperature and baryon chemical potential in comparison to the lattice data from Ref. [17]. The isospin densities are rescaled here to adjust to the lattice parameters. This mainly compensates for the larger pion mass and decay constant on the lattice.

Compared to that, a finite sigma mass $y < \infty$ in the linear sigma model has the same qualitative effect as observed in the eMF results of Fig. 5 for parameter sets A, B and C in Tab. 2.

The general structure of the phase diagram in the $T = 0$ plane is also strongly constrained by the Silver Blaze property. The key to its understanding is the fact that different degrees of freedom couple to different combinations of the chemical potentials. While up(down)-quarks couple to $\mu \pm \mu_I$, charged pions obviously only couple to the isospin chemical potential μ_I. The partition function and, correspondingly, thermodynamic observables must remain independent of μ *and* μ_I as long as $\mu + \mu_I < m_q \equiv g\sigma_{\rm min} = g f_\pi$ and $\mu_I < m_\pi/2$, where m_q and m_π are the vacuum quark and pion masses, respectively. This defines a quadrilateral area in the zero-temperature phase diagram, which we refer to as the *first Silver Blaze region* in the following. The physical picture is that in absence of bound quark matter, the horizontal line in the (μ_I, μ) plane defines the boundary of this region beyond which a degenerate Fermi gas of up-quarks forms, just as the vertical line marks the onset of pion condensation. Another constraint arises inside the pion condensation phase: For $\mu_I > m_\pi/2$ the vacuum changes and the grand potential becomes μ_I-dependent, of course. Nevertheless, for constant μ_I, it has to remain independent of the isosymmetric quark chemical potential μ as long as this stays below the lightest quark mass, *i.e.*, for $\mu < m_q^-(\mu_I)$, where

$$m_q^\pm(\mu_I) = \sqrt{g^2 d^2 + (g\rho \pm \mu_I)^2} \qquad (23)$$

are the quark masses at $\mu = 0$. They no longer correspond to pure up- and down- quark excitations as these mix in the pion condensation phase, and the quark masses are obtained by diagonalizing $\Gamma_k^{(2,0)}$. More generally, from the quark dispersion relation

$$E_q^-(\vec{p}^2) = \sqrt{g^2 d^2 + \left(\sqrt{\vec{p}^2 + g^2\rho^2} - \mu_I \right)^2}, \qquad (24)$$

one furthermore notes that for $\mu_I > g\rho$ it becomes energeti-

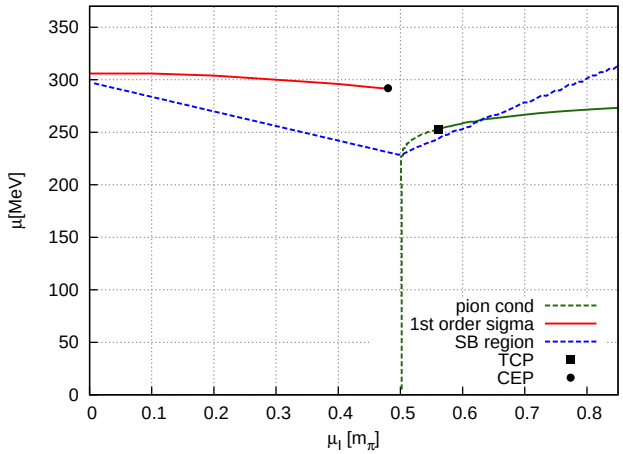

Figure 6: (μ_I, μ) phase diagram at $T = 0$ from an eMF calculation (parameter set A). The SB line marks the boundary of the first/second Silver Blaze region.

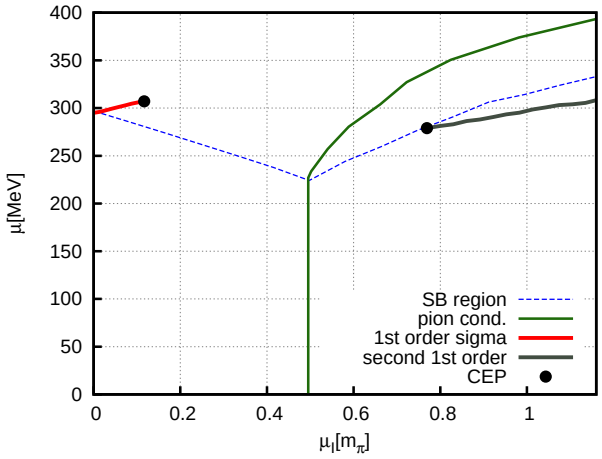

Figure 7: (μ_I, μ) phase diagram at $T = 0$ from the full FRG calculation (parameter set C). The SB line represents $\mu = m_q^-$.

cally favorable to excite quarks with a finite spatial momentum $\vec{p}^2 = \mu_I^2 - g^2\rho^2$ and minimal energy $E^-_{\rm min} = gd$ [37]. This might be an indication for an inhomogeneous phase at large isospin chemical potential such as the FFLO phases [27, 28] also discussed for two-color QCD with isospin chemical potential [59, 60] or in the 1+1 dimensional NJL model [61].

Therefore, the conditions $\mu_I > m_\pi/2$ with $\mu < m_q^-(\mu_I)$ for $\mu_I < g\rho$, or $\mu < E^-_{\rm min}$ for $\mu_I > g\rho$, together define a region in the zero-temperature phase diagram in which the μ_I-dependent grand potential still remains independent of μ, nevertheless. We will call this the *second Silver Blaze region* in the following.

Note however that the whole argument holds only as long as there are no first order transitions in these regions of the phase diagram. This concerns in particular the possible first order transition for large μ and small μ_I which may intersect with the first Silver Blaze region. If it does, the CEP where it ends must lie outside, however. This could then be the chiral first order transition or a liquid-gas transition to bound quark matter below the threshold for free quarks, for example, which are of course not excluded. In contrast, a first order line with an endpoint inside the Silver Blaze region would be thermodynamically inconsistent. It is reassuring that we never observe this in our numerical calculations either.

eMF calculation. Fig. 6 shows the phase diagram in the (μ_I, μ) plane from an eMF calculation. As discussed above, there is a chiral first order transition outside the pion condensation phase for large baryon chemical potential and small isospin chemical potential. With parameter set A, the first order transition lies completely outside the first Silver Blaze region bounded by $\mu + \mu_I < m_q$. The vertical line in the phase diagram separates the charged pion condensation phase from the normal chiral symmetry breaking phase. This phase boundary stays at the constant $\mu_I = m_\pi/2$ until $\mu > m_q - m_\pi/2$ from where on it bends to larger values of μ_I when further increasing μ. For $\mu_I > m_\pi/2$ the general arguments from above require the phase boundary of the pion condensation phase, as long as it is of second order, to stay outside the second Silver Blaze region. Indeed, in perfect agreement with these general arguments, the boundary of the pion condensation phase crosses the Silver Blaze line only after it has become of first order, beyond a tricritical point (TCP) as in Ref. [41], which is here observed at $(\mu_I, \mu) = (0.56\, m_\pi, 253\,\text{MeV})$. We will see, however, that this first order line gets washed out by the mesonic fluctuations.

At the mean-field level the Silver-Blaze property is manifest in the explicit expressions for the partition function. This has been observed in [42] as a property of the zero temperature partition function. It also holds for the explicit eMF expression for the effective potential Eq. (19): one verifies that it remains constant throughout the first Silver Blaze region with $\mu + \mu_I < m_q$ and $\mu_I < m_\pi$. Moreover, with Eq. (19), the condition for the second-order phase boundary of charged pion condensation,

$$\left.\frac{\partial U}{\partial d^2}(\mu_I^c)\right|_{\rho^2 = f_\pi^2,\, d^2 = 0} = 0, \tag{25}$$

which defines the critical isospin chemical potential $\mu_I^c(\mu)$, is in fact independent of μ for $\mu + \mu_I \leq g f_\pi \equiv m_q$. This implies that the boundary of the pion condensation phase stays constant at $\mu_I^c = m_\pi/2$ for $\mu < m_q - m_\pi/2$ as also seen in Fig. 6. In fact, Eq. (25) coincides with

$$\left.\Gamma_\pi^{(0,2)}(p;\sigma)\right|_{-p^2 = (2\mu_I^c)^2,\, \sigma = f_\pi} = 0, \tag{26}$$

from Eq. (20) there. This establishes explicitly that the pole mass agrees with the onset of pion condensation at $\mu_I^c = m_\pi/2$ for all $\mu < m_q - m_\pi/2$ in the eMF calculation.

FRG calculation. Fig. 7 shows the corresponding phase diagram from the full FRG calculation. As in mean-field calculations there is a first order transition at large μ and small μ_I. However, the mesonic fluctuations tend to weaken this first order transition and correspondingly the CEP is at a smaller μ_I than in eMF. For small chemical potential μ, the second order transition separating charged pion condensation from the normal χSB phase again occurs at $\mu_I = m_\pi/2$. And again, the phase boundary stays constant until it hits the first Silver Blaze boundary line at $\mu = m_q - m_\pi/2$, which defines the edge between the first and the second Silver Blaze region.

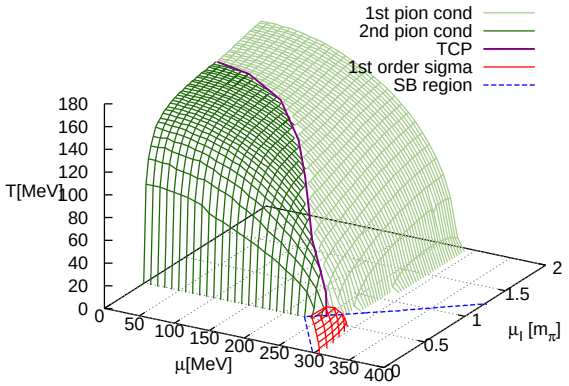

Figure 8: Three dimensional phase diagram from eMF (parameter set A).

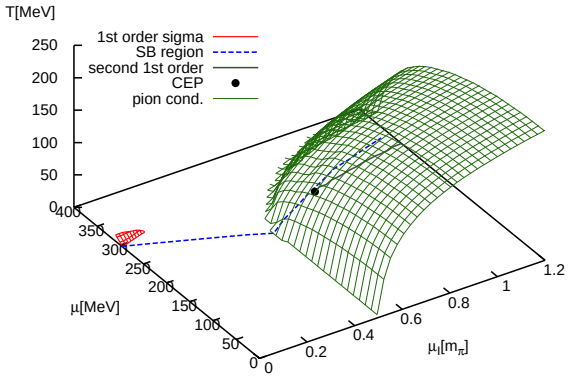

Figure 9: Three dimensional phase diagram from full FRG (parameter set C).

In contrast to mean-field calculations, however, the pion condensation transition with the mesonic fluctuations remains second order for the whole range of isospin chemical potentials we have investigated. Note also that this second order phase transition occurs outside the Silver Blaze region. Interestingly, one observes another first order transition inside this region for large isospin chemical potentials which was not present in the eMF calculation. This implies that the zero temperature partition function and correspondingly also the chiral and charged pion condensates at fixed μ_I stay independent of μ only below this first order transition line which seems to end in a CEP right at the boundary of the second Silver Blaze region.

4.4. Three dimensional (μ_I, μ, T) phase diagram

At finite temperature the phase boundaries in Figs. (6) and (7) extend into surfaces in the three dimensional parameter space with temperature T over the (μ_I, μ) plane. These are shown for a representative eMF calculation in Fig. 8, and a full FRG solution on the two-dimensional grid in field space with fluctuations in the chiral as well as the charged pion condensate in Fig. 9.

The green surfaces in these figures represent the boundary of the pion condensation phase. The zero temperature TCP of Fig. 6 in the eMF calculation extends into the purple line in Fig. 8, which divides the surface of the pion condensation transition into a second order region (dark green, smaller μ_I) and a first order region (light green, larger μ_I). At the other end of this purple tricritical line, in the (μ_I, T) plane at $\mu = 0$, it becomes the analogue of a TCP that was also predicted for two-color QCD at finite baryon chemical potential from next-to-leading order χPT [62]. For a better comparison with the corresponding QMD model mean-field results in [45], here we have removed the UV cutoff in the UV-finite thermal contributions to the fermionic flow. When a common UV cutoff scale is used for all fermionic fluctuations as in Eq. (19), on the other hand, this end of the tricritical line bends towards larger μ_I and away from the $\mu = 0$ plane. Including the full mesonic fluctuations of chiral and charged pion condensates we observe no first order pion condensation transition at all. The whole (light green) first order surface towards the larger μ_I values is gone, see Fig. 9, and with it the entire tricritical line. For $\mu = 0$ this is parallels the two-color case, in which the fluctuations due to collective mesonic and baryonic excitations were found to remove the tricritical point and the corresponding first order line [45].

The chiral first order line of the $T = 0$ eMF phase diagram for small μ_I, just outside the first Silver Blaze region in Fig. 6, is the baseline of the red surface in the corresponding three-dimensional eMF phase diagram in Fig. 8. Its edge represents the line of the critical endpoint in Fig. 4 which moves to lower temperature with increasing μ_I ending up as that in Fig. 6. As one can see from these figures, it thereby stays well clear of the pion condensation phase. The corresponding (red) first order surface with fluctuations in Fig. 9 shows a similar behavior, albeit being much smaller than in the eMF calculation as already observed at $T = 0$. This first order transition does not disappear but is considerably weakened by the fluctuations as well.

With fluctuations, there is another first order surface inside the pion condensation phase. This is the extension into the three dimensional parameter space with temperature of the first order line near the boundary of the second Silver Blaze region in Fig. 7. We have not investigated it in much detail here and it is not included in Fig. 9, but it rises only to relatively small temperatures ending in another line of critical endpoints similar to that of chiral first order transition, but entirely contained inside the pion condensation phase.

Finally, in Fig. 10 we show various (μ_I, T) planes for different values of the isosymmetric quark chemical potential μ of the FRG phase diagram with fluctuations in Fig. 9. The $\mu = 0$ plane thereby corresponds to the (μ, T) phase diagram of the QMD model for two-color QCD with diquark instead of charged pion condensation. This naturally reflects the precise map between the corresponding flow equations. Fig. 10 also shows how the chiral condensate vanishes as the vacuum rotates in the pion condensation phase. For small baryon chemical potentials, below the edge of the Silver Blaze regions at $\mu = m_q - m_\pi/2$, small quantitative changes arise at finite T. At larger μ the imbalance between the Fermi surfaces of up and anti-down quarks builds up, and the pion condensation phase starts to shrink rapidly, likely leading into an FFLO phase or alike in some possibly small region where both μ and μ_I are about equally large.

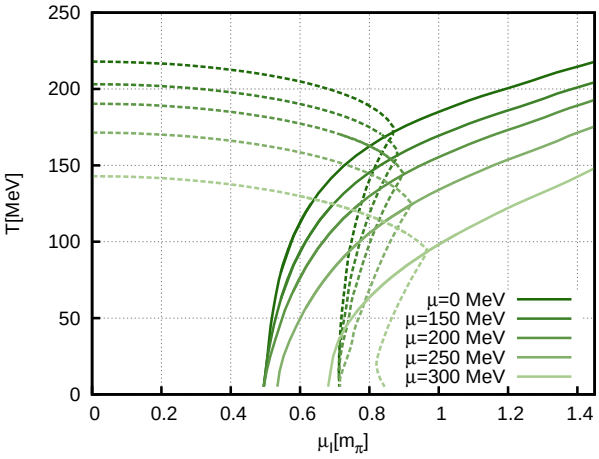

Figure 10: (μ_I, T) slices for different baryon chemical potentials of the three-dimensional FRG phase diagram in Fig. 9. Also shown here are chiral crossover lines (dashed) as the half-value of the chiral condensate.

5. Summary and Conclusions

We have investigated the phase diagram of the two-flavor QM model for QCD with both isospin and baryon chemical potential using the FRG. We showed explicitly how this effective model can be mapped onto the QMD model for two-color QCD. As compared to earlier NJL model studies, mesonic fluctuations are included with the FRG. We have demonstrated their effects on the phase diagram by detailed comparisons of purely fermionic flows in the eMF approximation with full FRG results. As compared to previous FRG studies, collective mesonic excitations are included in a way suitable to simultaneously describe the competing fluctuations in both, the chiral and the charged pion condensates, based on recent developments within the QMD model for two-color QCD. As compared to the latter, a finite baryon chemical potential here adds another dimension to the parameter space of the phase diagram. Without baryon chemical potential, our results compare well with recent lattice data indicating that the sigma might be important for the meson mixing and the change in the low-lying excitation spectrum over the BEC-BCS crossover in the pion condensation phase. At zero temperature, baryon chemical potentials below generalized Silver Blaze bounds have no effect. Beyond those, the increasing imbalance of the up and anti-down Fermi energies reduces pion condensation as expected. Moreover, the onset of pion condensation once more demonstrates how important it is to use proper pole masses rather than screening masses for a realistic parameter fixing in QM models. We have shown how to obtain good estimates for those from the FRG in a way that is consistent with the FRG calculation of the grand potential.

Acknowledgements

K.K. was supported by the Grant-in-Aid for JSPS Fellows (No. 22-3671) and by that for the Global COE Program "The Next Generation of Physics, Spun from Universality and Emergence." This work was supported by the Helmholtz International Center for FAIR within the LOEWE program of the State of Hesse, the Helmholtz Association Grant VH-NG-332, and the European Commission, FP7-PEOPLE-2009-RG No. 249203.

References

[1] P. Braun-Munzinger and J. Wambach, Rev. Mod. Phys. **81** (2009) 1031.
[2] B. Friman, C. Hohne, J. Knoll, S. Leupold, J. Randrup, R. Rapp and P. Senger, Lect. Notes Phys. **814** (2011) 1.
[3] K. Fukushima and T. Hatsuda, Rept. Prog. Phys. **74** (2011) 014001.
[4] Ph. de Forcrand, PoS **LAT2009** (2009) 010.
[5] M. Buballa, Phys. Rept. **407** (2005) 205.
[6] K. Fukushima, Phys. Lett. B **591** (2004) 277.
[7] C. Ratti, M. A. Thaler and W. Weise, Phys. Rev. D **73** (2006) 014019.
[8] J. Berges, D. Jungnickel and C. Wetterich, Eur. Phys. J. C **13** (2000) 323.
[9] J. Braun, H.-J. Pirner and K. Schwenzer, Phys. Rev. D **70** (2004) 085016.
[10] B.-J. Schaefer and J. Wambach, Nucl. Phys. A **757** (2005) 479.
[11] B.-J. Schaefer, J. M. Pawlowski and J. Wambach, Phys. Rev. D **76** (2007) 074023.
[12] D. T. Son and M. A. Stephanov, Phys. Rev. Lett. **86** (2001) 592.
[13] J. B. Kogut, M. A. Stephanov, D. Toublan, J. J. M. Verbaarschot and A. Zhitnitsky, Nucl. Phys. B **582** (2000) 477.
[14] J. B. Kogut and D. K. Sinclair, Phys. Rev. D **70** (2004) 094501.
[15] D. K. Sinclair and J. B. Kogut, PoS LAT **2006** (2006) 147.
[16] Ph. de Forcrand, M. A. Stephanov and U. Wenger, PoS LAT **2007** (2007) 237.
[17] W. Detmold, K. Orginos and Z. Shi, arXiv:1205.4224 [hep-lat].
[18] A. Nakamura, Phys. Lett. B **149** (1984) 391.
[19] S. Hands, J. B. Kogut, M. P. Lombardo and S. E. Morrison, Nucl. Phys. B **558** (1999) 327.
[20] S. Hands, *et al.*, Eur. Phys. J. **C17** (2000) 285-302; S. Hands, I. Montvay, L. Scorzato, and J. Skullerud, Eur. Phys. J. **C22** (2001) 451-461.
[21] S. Hands, P. Kenny, S. Kim and J. I. Skullerud, Eur. Phys. J. A **47** (2011) 60.
[22] K. Holland, P. Minkowski, M. Pepe and U. J. Wiese, Nucl. Phys. B **668** (2003) 207.
[23] A. Maas, L. von Smekal, B. Wellegehausen and A. Wipf, arXiv:1203.5653 [hep-lat].
[24] L. von Smekal, Nucl. Phys. B (Proc. Suppl.) **228** (2012) 179-220.
[25] J. Braun, L. M. Haas, F. Marhauser and J. M. Pawlowski, Phys. Rev. Lett. **106** (2011) 022002.
[26] J. M. Pawlowski, AIP Conf. Proc. **1343** (2011) 75.
[27] M. G. Alford, J. A. Bowers and K. Rajagopal, Phys. Rev. D **63** (2001) 074016.
[28] P. Fulde and R. A. Ferrell, Phys. Rev. **135** (1964) A550; A. I. Larkin and Y. N. Ovchinnikov, Zh. Eksp. Teor. Fiz. **47** (1964) 1136 [Sov. Phys. JETP **20** (1965) 762].
[29] M. Hanada and N. Yamamoto, JHEP **1202** (2012) 138.
[30] D. T. Son and M. A. Stephanov, Phys. Atom. Nucl. **64** (2001) 834 [Yad. Fiz. **64** (2001) 899].
[31] M. C. Birse, T. D. Cohen and J. A. McGovern, Phys. Lett. B **516** (2001) 27.
[32] B. Klein, D. Toublan and J. J. M. Verbaarschot, Phys. Rev. D **68** (2003) 014009.
[33] T. Kanazawa, T. Wettig and N. Yamamoto, JHEP **1112** (2011) 007.
[34] T. D .Cohen, Phys. Rev. Lett. **91** (2003) 222001; arXiv:hep-ph/0405043.
[35] A. Barducci, R. Casalbuoni, G. Pettini and L. Ravagli, Phys. Rev. D **69** (2004) 096004.
[36] L. -y. He, M. Jin and P. -f. Zhuang, Phys. Rev. D **71** (2005) 116001.
[37] D. Ebert and K. G. Klimenko, J. Phys. G G **32** (2006) 599.
[38] Z. Zhang and Y. X. Liu, Phys. Rev. C **75** (2007) 064910.
[39] S. Mukherjee, M. G. Mustafa and R. Ray, Phys. Rev. D **75** (2007) 094015.
[40] J. Xiong, M. Jin and J. Li, J. Phys. G **36** (2009) 125005.
[41] J. O. Andersen and L. Kyllingstad, J. Phys. G **37** (2009) 015003.
[42] T. Sasaki, Y. Sakai, H. Kouno and M. Yahiro, Phys. Rev. D **82** (2010) 116004.
[43] C. -f. Mu, L. -y. He and Y. -x. Liu, Phys. Rev. D **82** (2010) 056006.
[44] J. I. Kapusta and C. Gale, *Cambridge, UK: Univ. Press* (2006) 428 pp.
[45] N. Strodthoff, B.-J. Schaefer and L. von Smekal, Phys. Rev. D **85** (2012) 074007.
[46] C. Wetterich, Phys. Lett. B **301** (1993) 90.
[47] J. Berges, N. Tetradis and C. Wetterich, Phys. Rept. **363** (2002) 223.

[48] J. M. Pawlowski, Annals Phys. **322** (2007) 2831.
[49] D. F. Litim, Phys. Rev. **D64** (2001) 105007.
[50] T. Brauner, K. Fukushima and Y. Hidaka, Phys. Rev. D **80** (2009) 074035 [Erratum-ibid. D **81** (2010) 119904].
[51] J. P. Blaizot, R. Mendez-Galain and N. Wschebor, Phys. Rev. E **74** (2006) 051116.
[52] J. P. Blaizot, R. Mendez-Galain and N. Wschebor, Phys. Rev. E **74** (2006) 051117.
[53] D. Guerra, R. Mendez-Galain and N. Wschebor, Eur. Phys. J. B **59** (2007) 357.
[54] F. Benitez, R. M. Galain and N. Wschebor, Phys. Rev. B **77** (2008) 024431.
[55] T. Hatsuda and T. Kunihiro, Phys. Rev. Lett. **55** (1985) 158.
[56] V. Skokov, B. Friman, E. Nakano, K. Redlich and B. -J. Schaefer, Phys. Rev. D **82** (2010) 034029.
[57] E. E. Svanes, J. O. Andersen, Nucl. Phys. **A857** (2011) 16.
[58] B.-J. Schaefer and M. Wagner, Phys. Rev. D **79** (2009) 014018.
[59] K. Fukushima and K. Iida, Phys. Rev. D **76** (2007) 054004.
[60] J. O. Andersen and T. Brauner, Phys. Rev. D **81** (2010) 096004.
[61] D. Ebert, N. V. Gubina, K. G. Klimenko, S. G. Kurbanov and V. C. Zhukovsky, Phys. Rev. D **84** (2011) 025004.
[62] K. Splittorff, D. Toublan and J. J. M. Verbaarschot, Nucl. Phys. B **639** (2002) 524.